RSC Advances

PAPER

View Article Online
View Journal | View Issue

Cite this: *RSC Adv.*, 2014, **4**, 34552

Enhancing thermoelectric properties of a p-type Mg_3Sb_2- based Zintl phase compound by Pb substitution in the anionic framework†

A. Bhardwaj and D. K. Misra*

Received 23rd May 2014
Accepted 31st July 2014

DOI: 10.1039/c4ra04889j

www.rsc.org/advances

Mg_3Sb_2-based Zintl compounds have recently attracted attention as a potential candidate for thermoelectric applications due to their low thermal conductivity and promising thermoelectric performance (*i.e.* ZT = 0.6 at 773 K in $Mg_3Sb_{2-x}Bi_x$). We have reported previously that isoelectronic Bi^{3-} substitution of Sb^{3-} leads to a moderate increase in the electrical conductivity, enhanced Seebeck coefficient and reduced thermal conductivity. Herein, we report a large enhancement of the electrical conductivity while maintaining the Seebeck coefficient by substituting Pb^{4-} on Sb^{3-} sites in $Mg_3Sb_{2-x}Pb_x$ ($0 \leq x \leq 0.3$) alloys. Transport measurements reveal that optimum doping of 10 at% Pb^{4-} on Sb^{3-} enhances the ZT to 0.84 at 773 K which is comparable to bismuth telluride and selenide industrial materials which are toxic and expensive. The enhancement in ZT is attributed to a decrease in lattice thermal conductivity and simultaneously an increase in the power factor resulting from the significant increase in the electrical conductivity. We observe that Pb^{4-} substitutions on Sb^{3-} sites in $Mg_3Sb_{2-x}Pb_x$ ($0 \leq x \leq 0.3$) increase the hole carrier concentration. Electronic transport data of $Mg_3Sb_{2-x}Pb_x$ ($0 \leq x \leq 0.3$) alloys have been analyzed using a single parabolic band model and have been compared to Mg_3Sb_2. The relatively high figure of merit and affordable material ingredients coupled with one step synthesis process makes these materials a promising cost effective solution as thermoelectric materials.

1. Introduction

In recent years there has beena tremendous amount of effort to identify high performance thermoelectric materials based on inexpensive and relatively abundant constituents for application in power generation and refrigeration in various electronic devices.[1,2] Many applications of thermoelectric devices can be envisioned. However, their widespread implementation is restricted because of the poor performance of thermoelectric materials. Thermoelectric material performance is primarily determined by a dimensionless quantity, the so called thermoelectric figure of merit, $ZT = \frac{\alpha^2\sigma}{\kappa}T$, where α represents the Seebeck coefficient, σ is the electrical conductivity, T is the absolute temperature and κ (*i.e.* $\kappa = \kappa_{el} + \kappa_{lattice}$) is the thermal conductivity accounting both the electrical (κ_{el}) and lattice (κ_l) contributions.[3]

Thus high ZT materials must possess large α, high σ and low κ values and is rather difficult to optimize all these parameters simultaneously in the bulk conventional crystalline materials. However, several reports show that a partial decoupling between these parameters can be achieved by adapting several strategies namely (1) doping mechanism[4–7] (2) nanostructuring/nanocomposite[8–12] and (3) ideally engineered materials[13–17] with the electronic properties of a crystal and low thermal conductivity of a glass, the so called phonon glass electron crystal (PGEC). Following these concepts, in the last decade, many materials such as Bi_2Te_3,[12,18–21] $AgPb_mSbTe_{2+m}$ (LAST),[14] TeAgGeSb,[15] PbTe,[16,22] SiGe[17,23] and Zintl phase compounds[5,7,24–38] have been widely investigated for their high ZT. Among several classes of compounds, the Zintl phase is a unique class of materials that possesses the structural characteristics needed for phonon-glass electron-crystal properties (PGEC)[39] leading to a high thermoelectric figure of merit (ZT).[40,41] They combine distinct regions of covalent bonding ideal for electron-crystal properties and ionically bonded cations that can be easily substituted for precise tuning of electronic properties. This leads to the desired "electron crystal" behavior.[40,42] The complex structures and disorder creates phonon-glass properties resulting in low lattice thermal conductivity, making many Zintl compounds natural "phonon glasses".[43,44] As a consequences of these behaviors, a varieties of Zintl phase compounds such as $Yb_{14}MnSb_{11}$,[24] Zn_4Sb_3,[25] $Yb_9Mn_{4.2}Sb_9$,[26] filled skutterudites,[27,28] clathrates,[29,30] $YbZn_2Sb_2$,[31] $YbCd_2Sb_2$,[32] $BaZn_2Sb_2$,[33] $BaGa_2Sb_2$,[34] $Eu_5In_2Sb_6$,[35] $Yb_5In_2Sb_6$,[36] $EuZn_2Sb_2$,[37] AZn_2Sb_2[38] *etc.* with high ZT materials compared to other state-of-the-art thermoelectric

CSIR-Network of Institutes for Solar Energy, Materials Physics & Engineering Division, CSIR-National Physical Laboratory, Dr K.S. Krishnan Marg, New Delhi-110012, India. E-mail: misradk@nplindia.org; dakkmisra@gmail.com

† Electronic supplementary information (ESI) available. See DOI: 10.1039/c4ra04889j

materials have been explored. However, the use of expensive rare earth elements and toxic in majority of Zintl phase materials limits their use in large scale industrial application for power generation and refrigeration.

Among several Zintl phase compounds, Mg_3Sb_2 based materials involve a rare-earth free, non-toxic, cheap and abundant constituent which makes them economic and environmentally friendly utilization in power generation. Moreover, these compounds have been recognized as a potential candidate for lithium battery,[45] photoconduction,[46] hydrogen transmitting[47] and structural applications.[48] A Zintl phase compound of Mg_3Sb_2 crystallizes both in cubic bixbyite as well as in hexagonal structures.[49] The cubic bixbyite structure is α-phase of La_2O_3-type which is the high temperature phase, structured with 80 atoms unit cell with 48 Mg and 32 Sb atoms. At low temperature, below ~1200 K, Mg_3Sb_2 crystallizes to Mn_2O_3 type β-phase with unit cell composed of 5 atoms (3 Mg and 2 Sb). The β-phase hexagonal structure (space group $P\bar{3}m1$ no. 164) consists of two inequivalent Mg sites, denoted as Mg(I) and Mg(II) which are ionic and covalent in nature respectively. Thus, the bonding characteristic of Mg_3Sb_2 is in between metallic and ionic.[50,51] Similar to the structure of $CaAl_2Si_2$ structure, the stoichiometric Mg_3Sb_2 compound consists of interspersed $Mg_2Sb_2^{2-}$ layers (the tetrahedral position in the lattice) and Mg^{2+} cation layers (the octahedral position in the lattice).[52]

The thermoelectric properties of Mg_3Sb_2 have been studied by several groups.[53–56] However, due to difficulties in synthesizing hexagonal single phase of Mg_3Sb_2 by using conventional synthesis routes (*e.g.* ball milling and furnace reaction followed by hot-pressing) presence of measurable content of oxygen at grain boundaries,[56] lack of micro structural details and presence of impurity phases of C and MgC_2 contaminated by graphite die used in hot-pressing[55] and more importantly inconsistencies in the transport properties (*e.g.* ZT ≈ 0.55 at 600 K by Kajikawa *et al.*[55] and ZT ≈ 0.21 at 875 K by Condron *et al.*[56]) no significant progress has been made towards its viability for thermoelectric applications. However, recently, Singh *et al.*[57] theoretically investigated the detailed electronic structure and transport properties of Zinlt phase Mg_3Sb_2 and a series of alloys ($AeMg_2$) Pn_2 (Ae = Ca, Sr, Ba; Pn = As, Sb, Bi) compounds in relation to their thermoelectric performance. They claimed that the several promising compositions in this family are not fully optimized in terms of carrier concentration. The differences in electronic structure studied theoretically by them, suggest observing its accessibility by the experiments. Furthermore, several unanswered questions of fundamental nature as noticed from the previous studies,[53–56] combined with the relatively high abundance of constituents make this class of materials quite interesting and addresses the detail investigation.

Recently, we have studied the thermoelectric properties of single phase p-type Mg_3Sb_2 and its derivative of isoelectronic Bi doped; $Mg_3Sb_{2-x}Bi_x$ ($0 \le x \le 0.4$) alloys.[7] An enhanced ZT ≈ 0.6 at 773 K for p-type $Mg_3Sb_{1.8}Bi_{0.2}$ was realized by Bi^{3-} substitution on Sb^{3-}. Unfortunately, despite of high Seebeck coefficient and low thermal conductivity of Mg_3Sb_2, a moderate value of electrical conductivity was noted.[7] Herein, we report an enhancement in the electrical conductivity while maintaining the Seebeck coefficient by substituting Pb^{4-} on Sb^{3-} site in $Mg_3Sb_{2-x}Pb_x$ ($0 \le x \le 0.3$) alloys. The optimum doping of 10 at% Pb^{4-} on Sb^{3-} enhances the ZT to 0.84 at 773 K which is 40% and >200% larger over the $Mg_3Sb_{1.8}Bi_{0.2}$ (ZT ≈ 0.6 at 773 K)[7] and parent Mg_3Sb_2 (ZT ≈ 0.26 at 773 K)[7] compound respectively. We observe that Pb^{4-} substitutions on Sb^{3-} site in $Mg_3Sb_{2-x}Pb_x$ ($0 \le x \le 0.3$) yields a best control of carrier concentration for drastically improving the ZT. The high temperature electronic and thermal transport measurements combined with a single parabolic band model have been used to characterize the thermoelectric properties of $Mg_3Sb_{2-x}Pb_x$ ($0 \le x \le 0.3$) alloys.

2. Experimental procedures

Stoichiometric amounts of high purity elements magnesium (Mg; 99.99%, Alfa Aesar), antimony (Sb; 99.99%, Alfa Aesar), and lead (Pb; 99.99%, Alfa Aesar) for synthesizing $Mg_3Sb_{2-x}Pb_x$ ($0 \le x \le 0.3$) samples were blended in mechanical milling and subsequently grounded in an agate mortar. The blended powders were then subjected to spark plasma sintering (SPS) at temperature 1073 K and a pressure of 50 MPa for holding time of 10 minutes. The consolidated pellets were 12.7 mm diameter and 2.5 mm thick. The SPS were carried out by evacuating and flashing the SPS chamber with Ar gas several times and finally SPS were performed in high vacuum to avoid the oxidation. SPS eliminates adsorptive gas and impurities existing on the surface of the powder particles which results to very clean samples. The present synthesis strategy employing SPS involves simultaneous melting and consolidation of the stoichiometric $Mg_3Sb_{2-x}Pb_x$ ($0 \le x \le 0.3$) at high temperature and pressure following cooling to form relatively very small grains of single $Mg_3Sb_{2-x}Pb_x$ composition phase.

The gross structural characterization of $Mg_3Sb_{2-x}Pb_x$ ($0 \le x \le 0.3$) samples was carried out by powder X-ray diffractometer (Rigaku Mini Flex II) using a graphite monochromator and CuKα radiation with wavelength $\lambda \approx 1.5406$ Å along with $CuK\alpha_2$ filter and rotating anode equipped with powder 2θ diffractometer ranging from 20 to 80°. The microstructure and compositional analysis were investigated by field emission scanning electron microscopy (FE-SEM; Model: SUPRA40 VP, operating at 30 kV) equipped with energy dispersive spectroscopy (EDS) and transmission electron microscopy (TEM; Technai G^2 T^{30}; W-Twin) operating at 300 KV. The TEM specimens were prepared in three steps and described elsewhere.[7]

The polished SPSed pellets were used directly for thermal diffusivity measurements parallel to the pressing direction. Specific heat was determined by a DSC instrument (822^e Mettler Toledo). The thermal conductivity of the sample was calculated using the relation $\kappa = \alpha \times C_p \times \rho$, where κ is the thermal conductivity, α the thermal diffusivity, ρ the geometrical pellet density and C_p the specific heat capacity. The thermal diffusivity, specific heat and density measured for all samples, are presented in ESI S1, S2 and T1.† The polished bars of about 3 × 2 × 10 mm were cut from the consolidated disks and are used to measure the electrical conductivity and Seebeck coefficient in a direction perpendicular to the pressing direction. These bar

samples were also used for the thermal conductivity measurement to verify the isotropy of thermal properties.

3. Results and discussion

3.1 X-ray diffraction analysis

All the samples were identified for phase purity prior to any transport properties measurement and X-ray diffraction pattern performed on the SPSed samples are shown in Fig. 2(a) for each composition of $Mg_3Sb_{2-x}Pb_x$ ($0 \le x \le 0.3$) alloys. In compositions with $x < 0.30$, all the reflections can be indexed to β-Mg_3Sb_2 (JCPDS-00-003-0375) and no secondary phase is observed (Fig. 2(a)). However, the sample with nominal composition of $Mg_3Sb_{1.7}Pb_{0.3}$, reveals Pb as additional phase together with β-Mg_3Sb_2 which might have precipitated due to its limited solubility in Mg_3Sb_2. The cell constants were estimated by the POLSQ FORTRAN program[58] and were found increasing with increasing Pb concentration, being consistent with the Vegard's law as shown in Fig. 2(b). Thus, all the samples of $Mg_3Sb_{2-x}Pb_x$ ($0 \le x \le 0.2$) are solid solution phase. It is noteworthy that the increase in the lattice parameters is observed to be consistent with the increasing ionic radii of Pb ions, while the broadening of the peaks is attributed to local strain due to heavier Pb substitution in the Sb sub lattice of Mg_3Sb_2 or due to disorder scattering. No additional peaks other than β-Mg_3Sb_2 peaks in the XRD spectrum of $Mg_3Sb_{2-x}Pb_x$ ($0 \le x \le 0.2$) were observed, confirming unambiguously the solubility of Pb in the anionic Sb sub-lattice. A solubility of 10 at% Pb in anionic Sb site in Mg_3Sb_2 observed may be expected similar to other reports.[59–61]

3.2 Scanning electron microscopy

In order to confirm the phase purity at microscopic scale, homogeneities and compositional analysis of β-$Mg_3Sb_{2-x}Pb_x$ ($0 \le x \le 0.3$), Field emission-Scanning electron microscopy (FE-SEM) investigation was carried out. The homogeneities of samples $Mg_3Sb_{2-x}Pb_x$ ($0 \le x \le 0.2$) were assessed by averaging the compositions at 4 different regions of each sample obtained by Energy dispersive X-ray analysis (EADX). The average value of composition is shown in Table 1 marked as SEM-EDAX compositions. All the samples show macroscopically homogeneous as revealed by SEM-EADX analysis given in Table 1. Fig. 3 represents SEM investigation of Mg_3Sb_2 and $Mg_3Sb_{1.8}Pb_{0.2}$ alloys. Morphological evidences as presented in Fig. 3(a) and (d) for Mg_3Sb_2 and $Mg_3Sb_{1.8}Pb_{0.2}$ respectively show almost similar appearance of microstructures. Energy dispersive spectrum mapping combined with SEM-EDAX was recorded to see qualitatively the presence of any minor impurity other than Mg & Sb and the results are shown in Fig. 3(b). It can clearly be seen that only Mg and Sb, were present in their respective concentrations. Fig. 3(c) represent SEM-EADX spectrum of Mg_3Sb_2 sample recorded from a region marked by rectangle (Fig. 3(a)), clearly witnessed the presence of only Mg and Sb. Quantification results estimated from the spectrum (inset Fig. 3(c)) clearly reveals the Mg_3Sb_2 composition. Similar investigation such as SEM- imaging, SEM-mapping and SEM – EADX for $Mg_3Sb_{1.8}Pb_{0.2}$ have been presented in Fig. 3(d)–(f) respectively showing homogeneities in terms of composition (see Table 1), all the element; Mg, Sb & Pb in their respective concentration as shown in EDAX-mapping (Fig. 3(e)) and SEM-EDAX spectrum and quantification (Fig. 3(f)) with composition very close to the nominal composition of $Mg_3Sb_{1.8}Pb_{0.2}$ alloy.

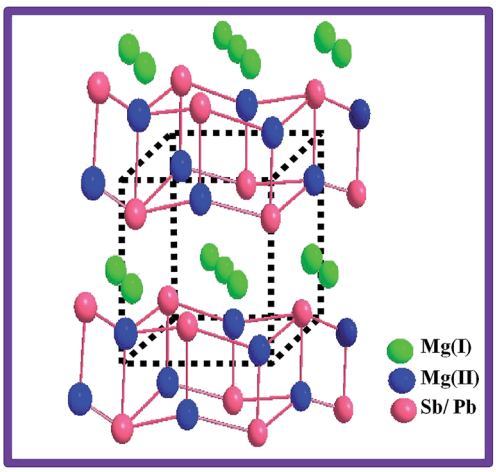

Fig. 1 Schematic diagram of layered crystal structure of $Mg_3Sb_{2-x}Pb_x$ showing the anionic framework of $[Mg_2\ (Sb/Pb)_2]^{2-}$ with double layer and Mg^{2+} cations between the layers.

3.3 Transmission electron microscopy investigation

The detail microstructures at lattice scale of Mg_3Sb_2 and $Mg_3Sb_{1.8}Pb_{0.2}$ alloys have been carried out by high resolution transmission electron microscopy (HR-TEM). In general bright field electron micrographs obtained from the specimen of Mg_3Sb_2 exhibits a polycrystalline structure throughout the volume of the material (Fig. 4(a)). A corresponding selected area electron diffraction pattern (SAEDP) as shown in Fig. 4(b) reveals a set of Debye rings with fine sharp spots overlapping on individual rings. The analysis of these rings reveals that the material consists of a single phase Mg_3Sb_2 with lattice planes, with lattice planes, *hkl*: $11\bar{2}0$, $20\bar{2}0$, $11\bar{2}4$, $21\bar{3}3$ having inter planer spacing of 0.229, 0.198, 0.142, 0.127 nm respectively, of hexagonal crystal structure with lattice parameter $a = 4.58$ A, $c = 7.24$ A (space group $P\bar{3}m1$). At low magnification (Fig. 4(a)), the micrograph shows grains with different sizes ranging from 8 nm to 80 nm and significant variation in grey contrast. The elemental composition of Mg_3Sb_2 sample estimated from energy dispersive spectroscopy analysis (EDAX) attached with TEM (Fig. 4(c)) reveals the composition very close to the nominal composition of Mg_3Sb_2 alloy. Several lattice scale images were recorded to understand the presence of different orientations of the crystallographic planes and their interface boundaries at atomic level. Fig. 4(d) presents high resolution transmission electron micrograph (HRTEM) image obtained from sample showing several grains orientated in direction of different planes of Mg_3Sb_2 and several joint interface boundaries. The micrograph (Fig. 4(d)) clearly reveals that the individual grains are truly crystalline with stacking of different

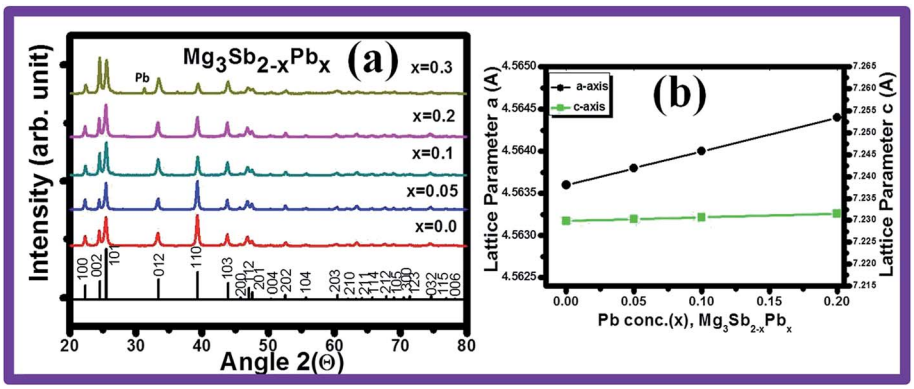

Fig. 2 (a) X-ray diffraction (XRD) pattern of $Mg_3Sb_{2-x}Pb_x$ ($0 \le x \le 0.3$) alloys. The XRD pattern reveals a single β-Mg_3Sb_2 type Zintl phase solid solution upto $x = 0.2$. The Pb peaks were noted for $x = 0.3$ together with β-Mg_3Sb_2. (b) Plot for Vegard's law following linear trend of cell parameters with increasing Pb concentration showing complete solid solution phase formation of $Mg_3Sb_{2-x}Pb_x$ ($0 \le x \le 0.2$) alloys.

Table 1 Contains the Hall measurement data and SEM-EDAX composition of $Mg_3Sb_{2-x}Pb_x$ ($0 \le x \le 0.3$) alloys

Nominal composition	Actual composition (SEM-EDAX)	Hall coefficient (R_H) × 10^{-2} cm^3 C^{-1}	Carrier conc. n (10^{20} cm^{-3})	Mobility μ (cm^2 V^{-1} s^{-1})
Mg_3Sb_2	$Mg_{60.29}Sb_{39.71}$	5.02	1.2	11
$Mg_3Sb_{1.95}Pb_{0.05}$	$Mg_{59.82}Sb_{38.96}Pb_{1.12}$	2.08	2.9	11.4
$Mg_3Sb_{1.90}Pb_{0.10}$	$Mg_{59.96}Sb_{37.98}Pb_{2.06}$	1.67	3.6	11.7
$Mg_3Sb_{1.80}Pb_{0.20}$	$Mg_{60.24}Sb_{35.30}Pb_{4.46}$	1.04	5.8	12.1
$Mg_3Sb_{1.70}Pb_{0.30}$	$Mg_{60.34}Sb_{33.65}Pb_{6.01}$	0.39	15.5	12.9

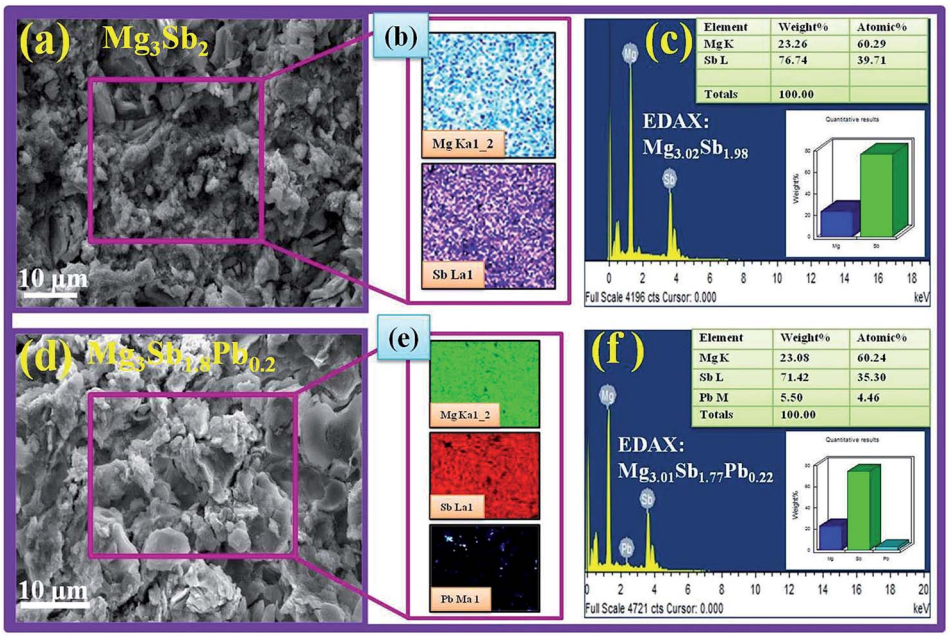

Fig. 3 FE-SEM micrographs of (a) Mg_3Sb_2 parent compound showing polycrystalline nature of sample (b) elemental EDAX mapping of Mg_3Sb_2 showing qualitatively the presence of constituent elements Mg and Sb (c) SEM-EADX of Mg_3Sb_2 confirming the composition, very close to Mg_3Sb_2 as shown in the inset (d) SEM image of $Mg_3Sb_{1.8}Bi_{0.2}$ revealing almost similar type morphology of Mg_3Sb_2 (e) elemental EDAX mapping images, demonstrating the presence of all three constituent elements; Mg, Sn and Pb (f) SEM-EADX of $Mg_3Sb_{1.8}Pb_{0.2}$ showing the same composition as the nominal composition (see inset).

planes and with random orientation with respect to each other. A bright field electron micrograph (Fig. 4(e)) corresponding to the specimen of $Mg_3Sb_{1.8}Pb_{0.2}$ shows a polycrystalline structure similar to Mg_3Sb_2 with relatively smaller grain sizes ranging from 5 nm to 60 nm. A corresponding SAEDP (not shown here) confirms β-Mg_3Sb_2 hexagonal structure. The lattice scale

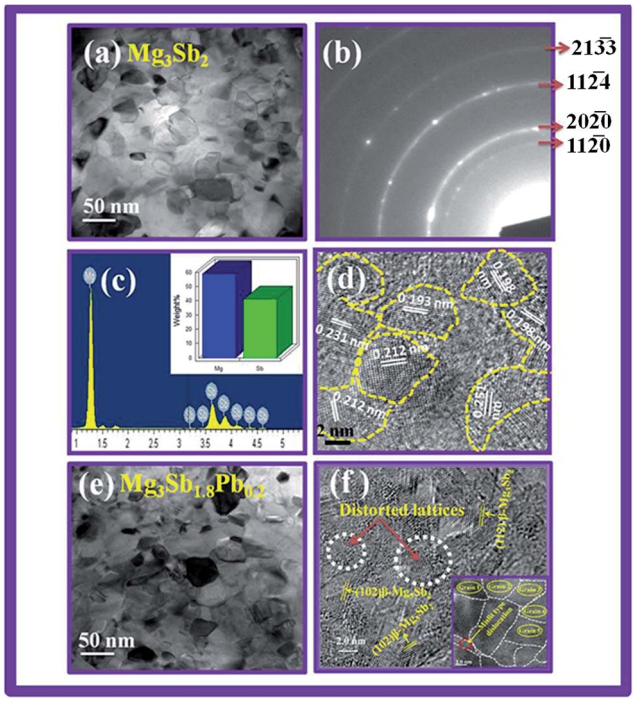

Fig. 4 (a) TEM image obtained from the specimen of Mg_3Sb_2 showing highly densified grains (b) SAED pattern corresponding to Mg_3Sb_2, revealing β-Mg_3Sb_2-type hexagonal structure, (c) EDS-TEM patterns recorded from Mg_3Sb_2 confirming its exact composition. (d) The lattice scale image of Mg_3Sb_2 exhibiting the presence of different orientations of the crystallographic planes and their interface boundaries. (e) Bright field electron micrograph recorded from the specimen of $Mg_3Sb_{1.8}Pb_{0.2}$ showing densely packed grains. (f) The lattice scale image of $Mg_3Sb_{1.8}Pb_{0.2}$ demonstrating distorted lattices. HRTEM image shown in the inset (f) exhibits misfit type of dislocation at the interfaces marked by arrow.

images reveals the randomly distributed grains with the inter planer spacing of the planes 112 (0.193 nm), 102 (0.27 nm) and many other planes of Mg_3Sb_2 hexagonal crystal structure (Fig. 4(f)). Interestingly, the lattices associated with grains of $Mg_3Sb_{1.8}Pb_{0.2}$ are observed to be little distorted together with some misfit-type of dislocations at the interfaces as marked by arrows in Fig. 4(f). The distortions in the lattices at microscopic level may be originated due to local strain due to substitution of heavy metal Pb at Sb site in the structure of Mg_3Sb_2.

3.4 Electronic transport properties

To determine the effect of Pb^{4-} substitution on Sb^{3-} site on the thermoelectric properties of $Mg_3Sb_{2-x}Pb_x$, high temperature electrical conductivity, Seebeck coefficient and thermal conductivity were measured. Fig. 5(a) displays the temperature dependence of electrical conductivity $\sigma(T)$, for different doping concentration of Pb in Mg_3Sb_2 alloy. Regardless of the temperature, the electrical conductivity increases with increasing Pb concentration. The $\sigma(T)$ increases monotonically with temperature for samples upto $x \leq 0.2$ over the entire temperature range of 323 K to 773 K, showing semiconducting behavior. Interestingly, for the case of $Mg_3Sb_{1.7}Pb_{0.3}$, $\sigma(T)$ decreases with rising temperature up to ~673 K showing a metallic behavior and further, above 673 K, it saturates indicating semi-metallic characteristics. Thus increasing Pb concentration in Mg_3Sb_2 leads to a transition from semiconducting to metallic behavior. The room temperature measurements of the Hall coefficient (R_H) were used to determine a Hall carrier concentration ($n_H = 1/R_He$) for all x-values in $Mg_3Sb_{2-x}Pb_x$ ($(0 \leq x \leq 0.3)$). As observed in Fig. 5(b), carrier concentration increases linearly with x up to $x = 0.2$ and further a large increment of n_H for $x = 0.3$ was noted. The linear increase in carrier concentration with x upto $x = 0.2$ indicates that the Pb^{4-} is indeed substituting on Sb^{3-} site and a true solid solution exists across series $Mg_3Sb_{2-x}Pb_x$ ($0 \leq x \leq 0.2$) which is also confirmed by Vegard's law (Fig. 1(b)). The room temperature electrical conductivity, and carrier concentration n_H are used to calculate the room temperature mobility (μ) by a relation $\sigma = ne\mu$ and results are shown in Fig. 5(c). It is noted from the graph (Fig. 4(c)), that measured Hall nobilities at room temperature are around 11–13 $cm^2\,V^{-1}\,s^{-1}$, and are not changed significantly, leading to the assumption that the carrier concentration primarily dominates the electronic transport.

Fig. 5(d) and (e) represents the temperature dependent Seebeck coefficient and effect of room temperature charge carriers on the Seebeck coefficient of $Mg_3Sb_{2-x}Pb_x$ alloys respectively. The Seebeck coefficients of all the samples are positive, indicating holes as the majority carrier type, consistent with the positive carrier concentration obtained from room temperature Hall measurement as shown in Table 1. A decrease in the Seebeck coefficient with increasing carrier concentration (increasing x) is observed (Fig. 5(e)), following the $n^{-2/3}$ dependence in the eqn (1) for a degenerate semiconductor with energy independent scattering. The equation for the $\alpha(T)$ dependence on the carrier concentration can be described in the heavy doping regime as[62]

$$\alpha = \frac{8\pi^2 {K_B}^2}{3eh^2} m^* T \left(\frac{\pi}{3n}\right)^{\frac{2}{3}} \quad (1)$$

where m^* is the effective mass, T, the temperature and n, the carrier concentration. The linear dependence of α with temperature is found only at low temperature as is assumed in this model. The temperature dependent Seebeck coefficient of $Mg_3Sb_{2-x}Pb_x$ (Fig. 5(d)) initially increases with temperature and attain a peak at 650 K. With further increasing temperature, beyond 650 K, the thermal excitation of electrons in present case begins to reduce the thermopower (Fig. 5(d)). We speculate that the thermally excited electrons do not cause a reduction in the Seebeck coefficient within the measurement range below 650 K. However, a detail high temperature Hall effect over the entire temperature range should be carried out to understand the exact mechanism of electronic transport. Thus, we observe that both σ and α increases with increasing temperature. The electrical conductivity usually depends on both carrier concentration (n) and mobility (μ). With regard to increase α and σ, we infer that "n" may be decreasing but μ would be increasing with temperature. The simultaneous increase in sigma and S is not usually expected for semiconductors and would require band structure information as well as high

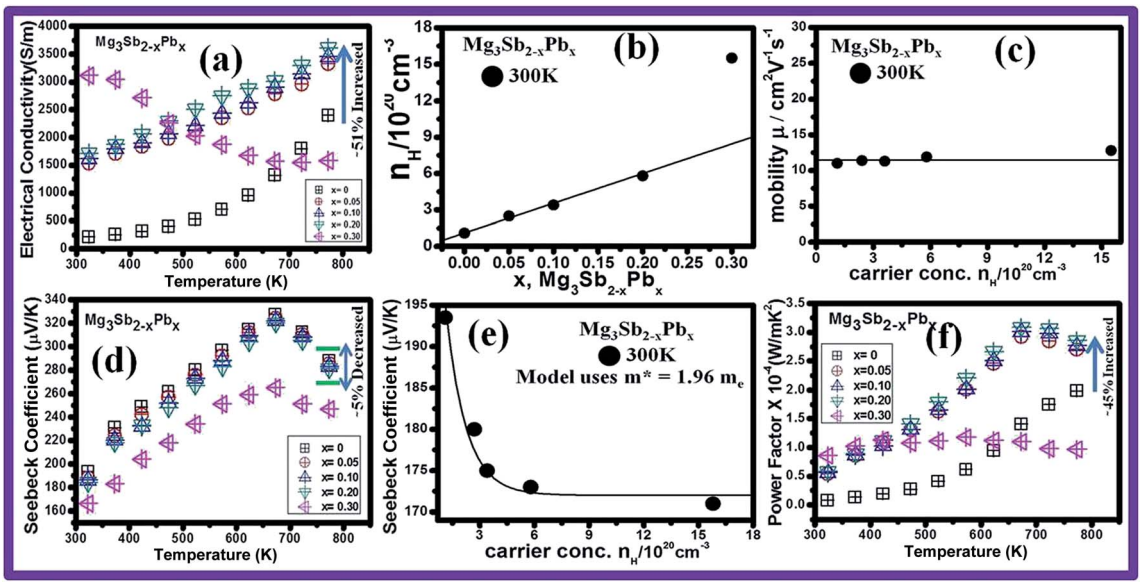

Fig. 5 (a) Temperature dependence of the electrical conductivity of $Mg_3Sb_{2-x}Pb_x$ (b) room temperature carrier concentration with increasing x (c) room temperature Hall mobility with increasing x (d) temperature dependence of the Seebeck coefficient, $\alpha(T)$; (e) Pisarenko plot at 300 K showing the dependence of Seebeck coefficient on the carrier concentration (solid line). The experimental data lie on or near the curve (single parabolic band model) generated for $m^* = 1.96\ m_e$ for $x = 0.2$, suggesting all the samples have almost equal effective masses (f) temperature dependent power factor, $(\sigma\alpha^2(T))$.

temperature Hall measurement to have better understanding.

The effective mass (m^*) of $Mg_3Sb_{2-x}Pb_x$ ($0 \le x \le 0.2$) were calculated from carrier concentrations (n) using eqn (1) and slope of Seebeck coefficient *versus* temperature plot. We noticed that effective mass remains almost unchanged across the solid solution of $Mg_3Sb_{2-x}Pb_x$ ($0 \le x \le 0.2$) which is not shown here. Further, assuming only one type of carrier at lower temperature with the assumption of the acoustic phonon scattering ($\lambda = 0$), a single parabolic model may be expected. The effective mass $m^* = 1.96\ m_e$ was used to calculate the Pisarenko relation at room temperature (Fig. 5(e)). The effective mass $m^* = 1.96\ m_e$ has been calculated from the experimental Seebeck and Hall carrier concentration for $x = 0.20$ at room temperature using eqn (1).

As evident from the Pisarenko plot shown in Fig. 5(e), the experimental Seebeck coefficient α and n_H fall on or near the curve corresponding to $m^* = 1.96\ m_e$ for $x = 0.2$, suggesting that a single parabolic band may be in good agreeing model for electronic transport of $Mg_3Sb_{2-x}Pb_x$ system at low temperatures where only one type of carrier exists. Based on the above analysis at low temperature, one can infer that substitution of Pb doesn't significantly alter the effective mass or mobility of the holes and thereby confirming the electronic transport is mainly monitored by the charge carrier densities.

The temperature dependence behavior of power factor of $Mg_3Sb_{2-x}Pb_x$ ($0 \le x \le 0.3$) is plotted in Fig. 5(f). Regardless of temperature, the power factor increases due to large increase in the electrical conductivity with increasing Pb concentration. However, with increasing temperature, the power factor for all the samples except $x = 0.3$ increases with rising temperature and maximized at 673 K. The highest power factor is optimized for $Mg_3Sb_{1.8}Pb_{0.2}$ at 673 K which is 45% larger than the parent Mg_3Sb_2 compound. We believe that Pb^{4-} substitution on Sb^{3-} site yields a best control over electrical conductivity and Seebeck coefficient in order to optimize high power factor.

3.5 Thermal transport properties

Fig. 6 shows the temperature dependence of thermal conductivity $\kappa(T)$ of $Mg_3Sb_{2-x}Pb_x$ alloys. As mentioned in the experimental section that the thermal conductivity are measured in a direction parallel to the pressing direction which is perpendicular to the direction in which the electronic transport is

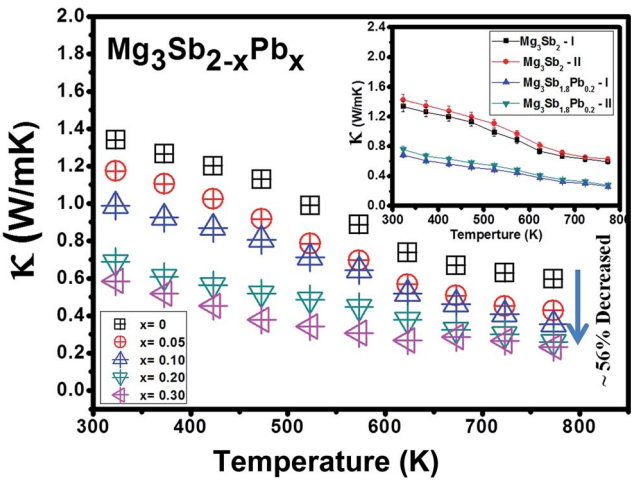

Fig. 6 Temperature dependence behaviour of the total thermal conductivity $\kappa(T)$ of $Mg_3Sb_{2-x}Pb_x$ ($0 \le x \le 0.3$).

measured. Additionally, the thermal conductivity measurements were performed on the rectangular bar specimens which were used for electrical transport. We find that the variation of about 5% in thermal conductivity, measured in parallel and perpendicular direction. This difference is not significant and lies within the equipment error suggesting near isotropic nature of sample. The isotropic nature could be attributed to the nano-sized powder of Mg_3Sb_2 and $Mg_3Sb_{1.8}Pb_{0.2}$ similar to the behavior in layered structure of Bi_2Te_3 nano-sized powder reported[12,21,63] where a variations of 5–10% in κ have been described and attributed to isotropic nature of Bi_2Te_3 sample in nanosized powder sample. Off course micron size powder always exhibit anisotropy which has been reported in layered structure of Bi_2Te_3 material.[64] Interestingly, the total thermal conductivity decreases with increasing Pb concentration in Mg_3Sb_2 alloy regardless to the temperature as shown in Fig. 6(a). Moreover, the total thermal conductivity, κ decreases with increasing temperature indicating $1/T$ type behavior, which is commonly occurred in the bulk crystalline solids. The lowest value of thermal conductivity is 0.23 W m^{-1} K^{-1} for $x = 0.3$ was observed which is attributed to mass fluctuations and grain boundary scattering due to increasing the Pb concentration. We have also verified the variation in thermal conductivity data by measuring the samples with thickness (~2.5 mm and 1 mm) to see the effect of heat dissipation on the thermal conductivity. However, only a little variation of 4–5% in κ was observed, which is presented in ESI S3.†

The temperature dependence of thermoelectric figure of merit, ZT of $Mg_3Sb_{2-x}Pb_x$ alloys is shown in Fig. 7. The maximum ZT ≈ 0.84 at 773 K was optimized for $Mg_3Sb_{1.8}Pb_{0.2}$ which is about >200% larger than the ZT value observed in parent Mg_3Sb_2 compound and 40% larger over $Mg_3Sb_{1.8}Bi_{0.2}$ of our previous report. The enhanced ZT is resulted from the significant increase in the electrical conductivity at little expense of Seebeck coefficient with further simultaneous decrease in the total thermal conductivity.

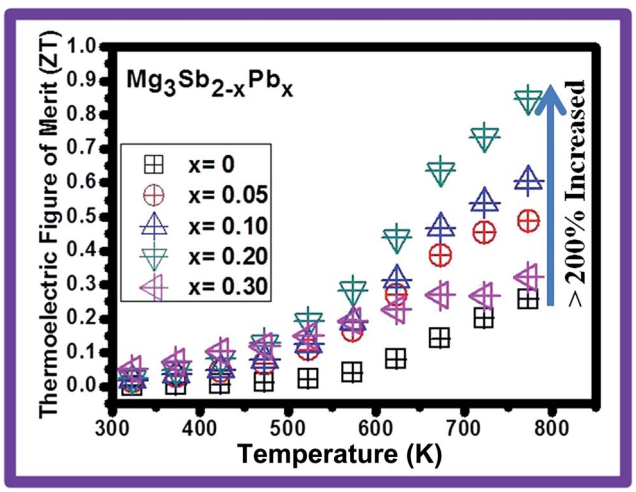

Fig. 7 Temperature dependence of thermoelectric figure of merit of $Mg_3Sb_{2-x}Pb_x$ ($0 \le x \le 0.3$).

4. Conclusions

A single solid solution Zintl phase of $Mg_3Sb_{2-x}Pb_x$ ($0 \le x \le 0.2$) was ascertained by characterizing the specimens employing XRD, FE-SEM and TEM investigation. Substitution of Pb^{4-} on Sb^{3-} site introduces holes as charge carriers, ascribed by Hall measurement data, and results into large p-type electrical conductivity. It was noted that the Pb substitution yields a best control over thermoelectric properties and does not significantly alter the effective mass or mobility and thereby confining the electronic properties to be mainly monitored by charge carrier densities. Electronic transports data of $Mg_3Sb_{2-x}Pb_x$ ($0 \le x \le 0.2$) alloys have been analyzed using a single parabolic band model at low temperature. The peak ZT ≈ 0.84 at 773 K has been achieved in $Mg_3Sb_{1.8}Pb_{0.2}$ alloy which is about >200% larger than the ZT value observed in parent Mg_3Sb_2 compound. The enhancement in ZT is due to increase in power factor resulted primarily by large increase in the electrical conductivity and with simultaneous decrease in the thermal conductivity. Additional enhancement in ZT could be expected to increase the power factor and reducing the lattice thermal conductivity by suitable doping. The present ZT value is comparable to with bismuth tellurides and selenides industrial materials which are toxic and expensive. Further, Mg_3Sb_2-based Zintl compounds being free from expensive rare earth elements, makes these materials cost-effective, environment friendly and abundant for the use of power generation.

Acknowledgements

This work was financially supported by CSIR-TAPSUN (CSIR-NWP-54) programme. The authors thank Prof. R. C. Budhani and Dr Jiji Pullikotil for useful discussions and comments. We acknowledge Dr Ajay Dhar (HOD, Metals and Alloys Group) for providing facilities and for his critical comments. Dr Sunil Pandey (NIMS University, Jaipur) is highly acknowledged for providing the room temperature Hall measurement equipment. One of the authors AB greatly acknowledges UGC-CSIR for financial support. We thank Radheshyam and Naval K. Upadhyay for technical and experimental support.

References

1 B. Raton, *CRC Handbook of Thermoelectrics*, CRC, Florida, USA, 1995.
2 H. J. Goldsmid, *Thermoelectric Refrigation*, Temple Press Books Ltd., London, 1964.
3 G. J. Snyder and E. S. Toberer, *Nat. Mater.*, 2008, **7**, 105.
4 Y. Pei, A. D. LaLonde, S. Iwanaga and G. J. Snyder, *Energy Environ. Sci.*, 2011, **4**, 2085–2089.
5 J. J. Pulikkotil, D. J. Singh, S. Auluck, M. Saravanan, D. K. Misra, A. Dhar and R. C. Budhani, *Phys. Rev. B: Condens. Matter Mater. Phys.*, 2012, **86**, 155204.
6 H. Wang, Y. Pei, A. D. LaLonde and G. J. Snyder, *Adv. Mater.*, 2011, **23**, 1366–1370.

7 A. Bhardwaj, A. Rajput, A. K. Shukla, J. J. Pulikkotil, A. K. Srivastava, A. Dhar, G. Gupta, S. Auluck, D. K. Misra and R. C. Budhani, *RSC Adv.*, 2013, **3**, 8504.
8 Y. Pei, J. L. Falk, E. S. Toberer, D. L. Medlin and G. J. Snyder, *Adv. Funct. Mater.*, 2011, **21**, 241–249.
9 D. K. Misra, A. Bhardwaj and S. Singh, *J. Mater. Chem. A*, 2014, **2**, 11913–11921.
10 A. Bhardwaj, D. K. Misra, J. J. Pulikkotil, S. Auluck, A. Dhar and R. C. Budhani, *Appl. Phys. Lett.*, 2012, **101**, 133103.
11 A. J. Minnich, M. S. Dresselhaus, Z. F. Ren and G. Chen, *Energy Environ. Sci.*, 2009, **2**, 466.
12 B. Poudel, Q. Hao, Y. Ma, Y. Lan, A. Minnich, B. Yu, X. Yan, D. Wang, A. Muto, D. Vashaee, X. Chen, J. Liu, M. S. Dresselhaus, G. Chen and Z. Ren, *Science*, 2008, **320**, 634.
13 Y. Pei, H. Wang and G. J. Snyder, *Adv. Mater.*, 2012, **24**, 6124.
14 K. F. Hsu, S. Loo, F. Guo, W. Chen, J. S. Dyck, C. Uher, T. Hogan, E. K. Polychroniadis and M. G. Kanatzidis, *Science*, 2004, **303**, 818.
15 J. Androulakis, K. F. Hsu, R. Pcionek, H. Kong, C. Uher, J. J. D'Angelo, A. Downey, T. Hogan and M. G. Kanatzidis, *Adv. Mater.*, 2006, **18**, 1170.
16 K. Ahn, K. Biswas, J. He, I. Chung, V. Dravid and M. G. Kanatzidis, *Energy Environ. Sci.*, 2013, **6**, 1529.
17 G. Joshi, H. Lee, Y. Lan, X. Wang, G. Zhu, D. Wang, R. W. Gould, D. C. Cuff, M. Y. Tang, M. S. Dresselhaus, G. Chen and Z. F. Ren, *Nano Lett.*, 2008, **8**, 4670.
18 S. Yu, J. Yang, Y. Wu, Z. Han, J. Lu, Y. Xie and Y. Qian, *J. Mater. Chem.*, 1998, **8**, 1949.
19 J. Shen, T. Zhu, X. Zhao, S. Zhang, S. Yanga and Z. Yina, *Energy Environ. Sci.*, 2010, **3**, 1519.
20 M. E. Anderson, S. S. N. Bharadwaya and R. E. Schaak, *J. Mater. Chem.*, 2010, **20**, 8362.
21 S. Sumithra, N. J. Takas, D. K. Misra, W. M. Nolting, P. F. P. Poudeu and K. L. Stokes, *Adv. Energy Mater.*, 2011, **1**, 1141.
22 J. R. Sootsman, H. Kong, C. Uher, J. J. D'Angelo, C. I. Wu, T. P. Hogan, T. Caillat and M. G. Kanatzidis, *Angew. Chem., Int. Ed.*, 2008, **47**, 8618.
23 R. Basu, S. Bhattacharya, R. Bhatt, M. Roy, S. Ahmad, A. Singh, M. Navaneethan, Y. Hayakawa, D. K. Aswal and S. K. Gupta, *J. Mater. Chem. A*, 2014, **2**, 6922.
24 S. R. Brown, S. M. Kauzlarich, F. Gascoin and G. J. Snyder, *Chem. Mater.*, 2006, **18**, 1873.
25 G. J. Snyder, M. Christensen, E. Nishibori, T. Caillat and B. B. Iversen, *Nat. Mater.*, 2004, **3**, 458.
26 S. K. Bux, A. Zevalkink, O. Janka, D. Uhl, S. Kauzlarich, J. G. Snyder and J. P. Fleurial, *J. Mater. Chem. A*, 2014, **2**, 215.
27 B. C. Sales, D. Mandrus and R. K. Williams, *Science*, 1996, **272**, 1325.
28 J. W. Graff, X. Zeng, A. M. Dehkordi, J. He and T. M. Tritt, *J. Mater. Chem. A*, 2014, **2**, 8933–8940.
29 G. S. Nolas, J. L. Cohn, G. A. Slack and S. B. Schujman, *Appl. Phys. Lett.*, 1998, **73**, 178.
30 H. Kleinke, *Chem. Mater.*, 2010, **22**, 604.
31 F. Gascoin, S. Ottensmann, D. Stark, S. M. Haile and G. J. Snyder, *Adv. Funct. Mater.*, 2005, **15**, 1860.
32 X. J. Wang, M. B. Tang, H. H. Chen, X. X. Yang, J. T. Zhao, U. Burkhardt and Y. Grin, *Appl. Phys. Lett.*, 2009, **94**, 092106.
33 X. J. Wang, M. B. Tang, J. T. Zhao, H. H. Chen and X. X. Yang, *Appl. Phys. Lett.*, 2007, **90**, 232107.
34 S. J. Kim and M. G. Kanatzidis, *Inorg. Chem.*, 2001, **40**, 3781.
35 S. M. Park, E. S. Choi, W. Kang and S. J. Kim, *J. Mater. Chem.*, 2002, **12**, 1839.
36 S. J. Kim, J. R. Ireland, C. R. Kannewurf and M. G. Kanatzidis, *J. Solid State Chem.*, 2000, **155**, 55.
37 H. Zhang, J. T. Zhao, Y. Grin, X. J. Wang, M. B. Tang, Z. Y. Man, H. H. Chen and X. X. Yang, *J. Chem. Phys.*, 2008, **129**, 164713.
38 G. S. Pomrehn, A. Zevalkink, W. G. Zeier, A. van de Walle and G. J. Snyder, *Angew. Chem., Int. Ed.*, 2014, **53**, 3422.
39 G. A. Slack, in *CRC Handbook of Thermoelectrics*, CRC, New York, 1995.
40 S. M. Kauzlarich, *Chemistry, Structure, and Bonding of Zintl Phases and Ions*, VCH Publishers, New York, 1996.
41 S. M. Kauzlarich, S. R. Brown and G. J. Snyder, *Dalton Trans.*, 2007, 2099–2107.
42 A. M. Mills, R. Lam, M. J. Ferguson, L. Deakin and A. Mar, *Coord. Chem. Rev.*, 2002, **233**, 207.
43 G. A. Slack, *Solid State Physics*, Academic Press, New York, 1979.
44 E. S. Toberer, A. Zevalkink and G. J. Snyder, *J. Mater. Chem.*, 2011, **21**, 15843.
45 H. Honda, H. Sakaguchi, I. Tanaka and T. Esaka, *J. Power Sources*, 2003, **123**, 216.
46 P. Singh and K. K. Sarkar, *Solid State Commun.*, 1985, **55**, 439.
47 N. Nishimiya, A. Suzuki and S. Ono, *Int. J. Hydrogen Energy*, 1982, **7**, 741.
48 J. C. Viala, F. Barbeau, F. Bosselet and M. Peronnet, *J. Mater. Sci. Lett.*, 1998, **17**, 757.
49 M. M. Ripoll, A. Haase and G. Brauer, *Acta Crystallogr., Sect. B: Struct. Sci., Cryst. Eng. Mater.*, 1974, **B30**, 2006.
50 J. H. Slowik, *Phys. Rev. B: Solid State*, 1974, **10**, 416.
51 L. M. Watson, C. A. W. Marshall and C. P. Cardoso, *J. Phys. F: Met. Phys.*, 1984, **14**, 113.
52 C. Zheng, R. Hoffmann, R. Nesper and H. G. von Schnering, *J. Am. Chem. Soc.*, 1986, **108**, 1876.
53 J. H. Bredt and L. F. Kendall, *Proceedings—IEEE/AIAA*, 1966.
54 D. M. Verbrugge and J. B. J. Van Zytveld, *J. Non-Cryst. Solids*, 1993, **736**, 156.
55 T. Kajikawa, N. Kimura and T. Yokoyama, *Proceedings of the 22nd International Conference on Thermoelectrics*, 2003, p. 305.
56 C. L. Condron, S. M. Kauzlarich, F. Gascoin and G. J. Snyder, *J. Solid State Chem.*, 2006, **179**, 2252.
57 D. J. Singh and D. Parker, *J. Appl. Phys.*, 2013, **114**, 143703.
58 D. Keazler, D. Cahen and J. Lbers, *POLSQ FORTRAN program*, Northwestern University Evanston, IL, 1984.
59 X. Shi, Y. Pei, G. J. Snyder and L. Chen, *Energy Environ. Sci.*, 2011, **4**, 4086.
60 G. J. Tan, L. W. Liu, C. H. Chi, X. L. Su, S. Y. Wang, Y. G. Yan, X. F. Tang, W. Wong-Ng and C. Uher, *Acta Mater.*, 2013, **61**, 7693–7704.

61 A. F. May, E. F. Larsen and G. J. Snyder, *Phys. Rev. B: Condens. Matter Mater. Phys.*, 2010, **81**, 125205.
62 M. Cutler, J. F. Leavy and R. L. Fitzpatrick, *Phys. Rev.*, 1964, **133**, A1143.
63 Y. Ma, Q. Hao, B. Poudel, Y. Lan, B. Yu, D. Wang, G. Chen and Z. F. Ren, *Nano Lett.*, 2008, **8**, 2580–2584.
64 J. Jiang, L. D. Chen, S. Bai, Q. Yao and Q. Wang, *Scr. Mater.*, 2005, **52**, 347–351.